J. Fluid Mech. (2023), *vol*. 976, R3, doi:10.1017/jfm.2023.960

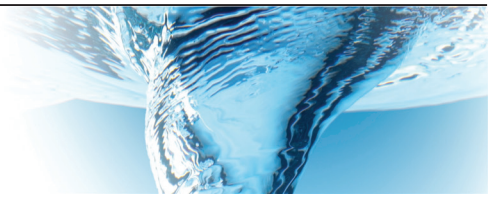

A data-driven analysis of short and long laminar separation bubbles

M. Dellacasagrande[1],†, D. Lengani[1], D. Simoni[1] and S. Yarusevych[2]

[1]Department of Mechanical, Energy, Management and Transport Engineering, University of Genoa, Genoa 16138, Italy

[2]Department of Mechanical and Mechatronics Engineering, University of Waterloo, Waterloo N2L 3G1, Canada

(Received 6 July 2023; revised 2 November 2023; accepted 9 November 2023)

This work investigates the statistical response of short and long laminar separation bubbles to external flow parameters, such as Reynolds number, free-stream turbulence intensity and streamwise pressure gradient, known to govern bubble formation and characteristics. A parametric experimental campaign has been performed using particle image velocimetry on a flat plate to provide a comprehensive database for the characterization of separation-induced transition in both short and long separation bubbles. The proper orthogonal decomposition (POD) was applied to the data set of all dividing streamlines commonly used to identify a laminar separation bubble. This provides an optimal state-space basis for the data-driven classification of the state of a laminar separation bubble, with the leading modes capturing the change in length and height of the laminar separation bubble in response to changes in the flow parameters. When projected onto the POD subspace constituted by the first three leading modes, the normalized data from the present study and the results from prior investigations not used in the modal analysis collapse on the same trajectory in the low-dimensional space. The present POD basis can be therefore adopted for the description of the general response of the time-mean shape of a laminar separation bubble to changes in the main influencing parameters. A well-defined pattern was observed in the case of short laminar separation bubbles in the reduced-order space defined by the first three POD coefficients, whereas a higher dispersion in the long-bubble regime indicates an increased sensitivity of long bubbles to the external flow characteristics.

Key words: boundary layer separation, boundary layer structure

† Email address for correspondence: matteo.dellacasagrande@edu.unige.it

1. Introduction

The response of a laminar separation bubble (LSB) to the change of the external flow characteristics has been investigated in a number of previous studies, e.g. Marxen & Henningson (2011), Hosseinverdi & Fasel (2019), Rodríguez, Gennaro & Souza (2021), Eljack *et al.* (2021), Toppings & Yarusevych (2022), Jaroslawski *et al.* (2023). At low Reynolds numbers and/or high angles of attack, the bursting process of an LSB may occur, causing an abrupt change of the bubble length due to a small variation in flow parameters. The occurrence of bursting leads to increased drag and reduced lift and consequently impedes the performance of wings and blades in relevant applications (Gaster 1967; Horton 1967). From a topological point of view, the bubble switches from a short to a long configuration, e.g. Marxen & Henningson (2011). Short bubbles induce a relatively minor, localized change in the surface pressure, with often acceptable performance penalties. In contrast, long bubbles lead to significant modification of the surface pressure distribution due to their relatively larger separated flow region (Sandham 2008).

From a dynamic point of view, the stability properties of an LSB change significantly between the short and the long states (e.g. Pauley, Moin & Reynolds 1990; Alam & Sandham 2000). Convective Kelvin–Helmholtz-type instabilities govern the onset of transition and the subsequent shear layer roll-up in short bubbles (e.g. Hosseinverdi & Fasel 2019). The formation of periodic vortices (Marxen, Lang & Rist 2013) and their successive three-dimensional breakdown then leads to the turbulent transition of the detached boundary layer (Marxen *et al.* 2013; Kurelek *et al.* 2021). It has been shown that global modes, for example, Rayleigh- and Görtler-type instabilities, may also cause transition to turbulence in the separated shear layer (e.g. Cherubini *et al.* 2010*b*). Previous studies have shown a notable dependence of LSB stability characteristics on the Reynolds number and the adverse pressure gradient (e.g. Alizard, Cherubini & Robinet 2009; Boutilier & Yarusevych 2012; Dellacasagrande *et al.* 2020), with the frequency of the most unstable harmonic perturbations decreasing as the Reynolds number and/or the pressure gradient increase. Using controlled perturbations in numerical and experimental works of Marxen & Henningson (2011) and Michelis, Yarusevych & Kotsonis (2017), respectively, it has been conjectured that varying levels of free-stream turbulence may lead to mean flow deformation (Marxen & Rist 2010) and, hence, LSB stability properties, which may induce bubble bursting.

When a long LSB forms over a lifting surface, absolute instability can dominate over the convective Kelvin–Helmholtz one (e.g. Rodríguez *et al.* 2021), with self-sustained modes driving the growth of fluctuations in the separated flow region (Balzer & Fasel 2016; Rodríguez *et al.* 2021). The occurrence of self-excited instability in LSBs has been documented in previous investigations(e.g. Pauley *et al.* 1990; Allen & Riley 1995; Hammond & Redekopp 1998; Rist & Maucher 2002; Fasel & Postl 2006; Embacher & Fasel 2014). Absolute instability has been shown to give rise to self-excited modes, which cause the formation of spanwise-oriented vortices (Huerre & Monkewitz 1990), whose breakup leads to turbulent transition. Self-sustained, two-dimensional, low-frequency fluctuations can occur in long LSBs, and their occurrence is accompanied by changes in the geometry of the separated flow region near the reattachment point (e.g. Marquillie & Ehrenstein 2003; Cherubini, Robinet & De Palma 2010*a*). Ehrenstein & Gallaire (2008) showed that at the onset of global instability vortical structures forming near the reattachment point become almost simultaneously unstable. The aforementioned investigations reveal a strong sensitivity of LSB stability characteristics to external flow properties and the time-mean topology of the separating boundary layer.

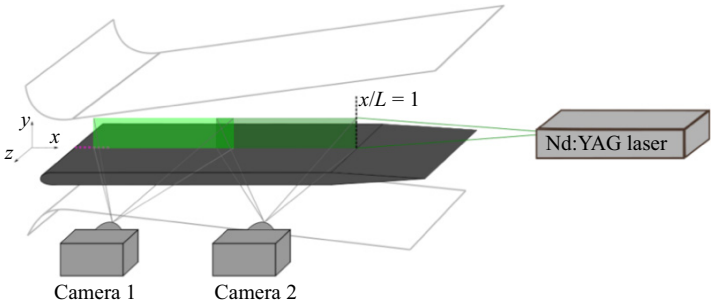

Figure 1. Test section and PIV instrumentation layout. Green boxes indicate the PIV measuring domain.

The identification of deterministic thresholds for the switch between short and long LSB regimes is of great importance for practical applications, due to the significant changes in lifting surface performance. Since the pioneering work of Gaster (1967), semiempirical correlations have been reported in the literature for the identification of the bubble state. Gaster (1967) suggested that the bursting condition may be described by the momentum thickness Reynolds number at separation and a pressure distribution parameter. Diwan, Chetan & Ramesh (2006) and Mitra & Ramesh (2019) modified Gaster's criterion, introducing the maximum bubble height as a parameter defining the bubble state (see also Serna & Lázaro 2015). All of the aforementioned studies provide valuable criteria for the occurrence of the bursting process with reference to several flow configurations. However, the path over which a short bubble bursts into a long one and the effects of the flow parameters on the scaling law of an LSB in either of the two regimes are yet to be investigated.

The present work aims at providing a low-dimensional representation of the statistical response of an LSB to the main influencing parameters via the modal decomposition of a large time-mean data ensemble. Experimental velocity data obtained over a broad parameter space are projected into an optimal state space provided by means of proper orthogonal decomposition (POD). A reduced order is obtained for a dividing streamline commonly used to outline an LSB and is used to demonstrate the existence of a general response of the LSB to changes in the influencing parameters, especially in the short-bubble regime. Furthermore, short and long LSBs can be identified clearly based on their position in the POD state space, thus showing the capability of the proposed method of providing a data-driven classification of the state of an LSB.

2. Experimental apparatus and measuring techniques

All measurements were performed in the wind tunnel installed in the Aerodynamic and Turbomachinery Laboratory at the University of Genova. Laminar separation bubbles were produced on a flat plate with an elliptic leading edge (4 : 1) positioned between two adjustable endwalls (see figure 1). Changing the endwall opening angle allowed varying of the adverse pressure gradient and hence LSB characteristics. The upstream part of the test section has a converging fixed geometry, while the streamwise pressure gradient can be changed over the rear part of the plate. For the present experiments, the opening angle of the diverging section was set to 9° and 12°. The corresponding values of the acceleration parameter defined as $AP = (L/U_{\infty,0})(\Delta U_\infty/\Delta x)$ are -0.27 and -0.41. Here, $\Delta U_\infty/\Delta x$ is the average velocity gradient along the rear part of the plate, $U_{\infty,0}$ is the free-stream velocity at the channel throat, and L is the length of the flat portion of the plate, which is equal to 300 mm. The plate width is also equal to 300 mm

Case	*Tu* (%)	*d* (mm)	*M* (mm)	*P*
No-grid	1.5 %	—	—	—
Low-*Tu*	2.5 %	2	8	0.56
High-*Tu*	3.5 %	4	8	0.25

Table 1. Turbulence-generating grids characterization: free-stream turbulence intensity (*Tu*), bars width (*d*), mesh size (*M*) and porosity parameter $P = (1 - (d/M))^2$.

producing 2-D time-average flow at mid-span. In order to mitigated trailing edge effects that may influence the evolution of LSBs (e.g. Nakamura, Ohya & Tsuruta 1991; Pröbsting & Yarusevych 2015), a 100 mm long trailing edge extension was employed (Verdoya *et al.* 2021). The extension was designed with a diffusing angle of approximately 5° to avoid geometrically induced boundary-layer separation. All LSBs considered in the present work were formed on the flat portion of the model. Two turbulence-generating grids located 500 mm upstream of the plate leading edge were used to vary the free-stream turbulence intensity level. The employed grids and resulting turbulence intensity levels are detailed in table 1. The *Tu* level was computed as the root mean square of streamwise velocity fluctuations measured via laser Doppler velocimetry at the plate leading edge. Velocity data were acquired at approximately 10 kHz over a sampling period of 120 s. For each combination of the *Tu* level and streamwise pressure gradient, 8 to 11 Reynolds numbers based on the plate length and the inlet free-stream velocity (Re_L) were tested. The overall test matrix consists of 52 flow cases producing unique LSBs.

Particle image velocimetry (PIV) measurements were performed in a wall-normal plane aligned with the meridional section of the plate (see the green boxes in figure 1). Two cameras with overlapping field of view were used to capture the boundary-layer development from the channel throat to the end of the plate, so as to quantify the evolution of LSBs forming over the plate surface. The PIV system includes a dual-cavity Nd:YAG pulsed laser Litron LDY 300 (energy 30 mJ per pulse at 1000 Hz repetition rate, 527 nm wavelength) and two SpeedSense M340 digital cameras with a cooled 2560 × 1600 pixels CMOS matrix. The magnification factor was set to approximately 0.16. The flow was seeded with Vaseline® oil droplets with a mean diameter of 1.5 μm. A multigrid algorithm was adopted for the computation of the adaptive cross-correlation of particle images. The final interrogation window of 16 × 16 pixels and 50 % overlap was used. This corresponds to a vector grid spacing of 0.41 mm. A peak validation was used to discriminate between valid and invalid vectors. Based on the work of Sciacchitano *et al.* (2015), the uncertainty in the instantaneous velocity is estimated to be smaller than 3 % and 6 % of U_0 in the free-stream and the boundary-layer region, respectively. For each combination of the flow parameters, two sets of 6000 snapshots were acquired at a sampling rate of 1 kHz and 300 Hz for the characterization of LSB dynamics and statistics, respectively.

3. Reynolds number effect on the time-mean shape and vortical structures of LSBs

Figure 2 depicts the time-average streamwise velocity contours for a high- (2*a*) and a low-Re_L (2*b*) case at fixed $Tu = 1.5\,\%$ and $AP = -0.41$. Vector maps of the instantaneous fluctuating velocity are also shown. Boundary-layer separation occurs at approximately $x/L = 0.42$ for both cases. The separation point was estimated via the extension of the

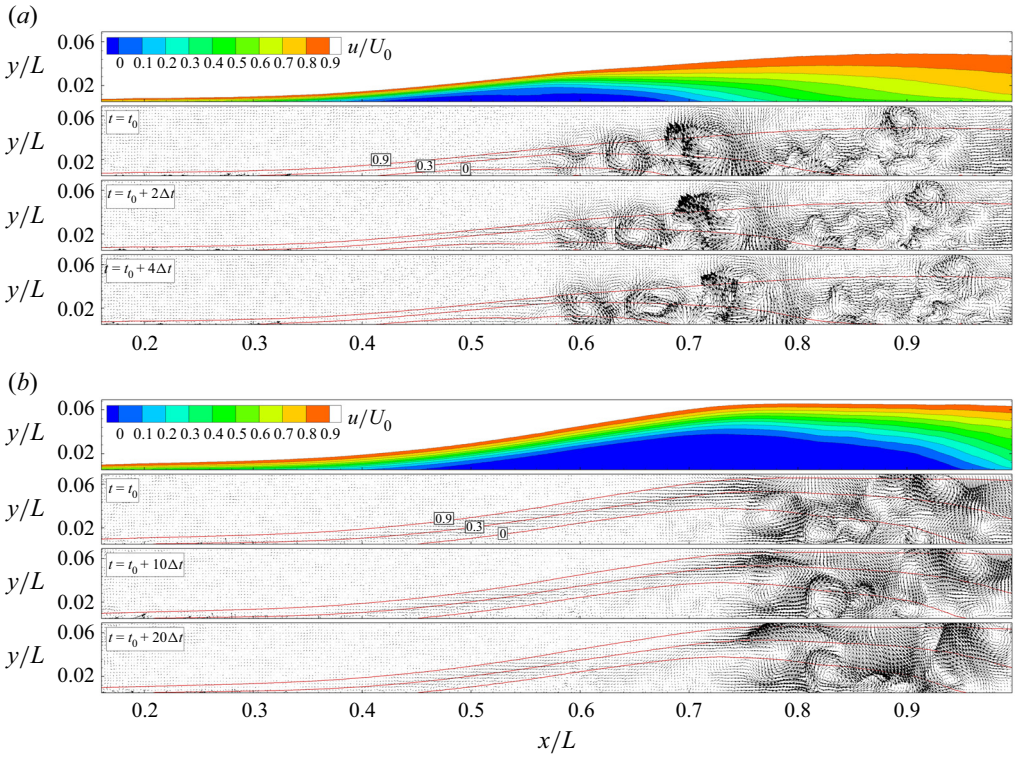

Figure 2. Contour plots of the normalized streamwise time-mean velocity u/U_0 (U_0 is the external velocity at the measuring domain inlet). Exemplary vector plots of the fluctuating velocity field are shown for each case with superimposed iso-lines of $u/U_e = 0,\ 0.3,\ 0.9$. (*a*) $Re_L = 66\,200$, $AP = -0.41$, $Tu = 1.5\,\%$. (*b*) $Re_L = 21\,000$, $AP = -0.41$, $Tu = 1.5\,\%$.

zero time-mean velocity line to the wall. At the higher Re_L, the separated shear layer reattaches to the wall at $x/L = 0.7$ and a short LSB is formed on the plate surface. The corresponding vector maps show the occurrence of a train of counter-rotating vortices becoming prominent in the aft portion of the LSB (Hosseinverdi & Fasel 2019). Vortical structures form in the high-shear region (see the iso-lines of the time-mean velocity) and grow in the streamwise direction. Farther downstream, the vortex breakup leads to the occurrence of smaller scale structures. For the lower Re_L case (figure 2*b*), the reattachment point moves to $x/L = 0.95$, and a long bubble forms. The isoline $u/U_0 = 0$ features a milder negative slope within $0.75 < x/L < 0.9$, past the maximum height location, notably lengthening the aft portion of the bubble. While the main shear layer roll-up is still seen in the high-shear region at approximately the maximum bubble height location, vortical structures can also be observed in the reverse-flow region and appear to amplify while they propagate upstream. This is indicative of self-sustained oscillations, as shown in Rodríguez *et al.* (2021). The same modification of the topology and dynamics of LSBs described here was observed for all the *Tu* levels and pressure gradients with reducing the Reynolds number, highlighting common features within the same bubble regime.

In order to provide an overview of the bubble response to the flow parameter variation, figure 3(*a*) reports all the dividing streamlines computed from the present data set. The height of the dividing streamline (h) is non-dimensionalized with the plate length, and the origin is set at the separation position (x_{sep}). Instead, in figure 3(*b*) the length and

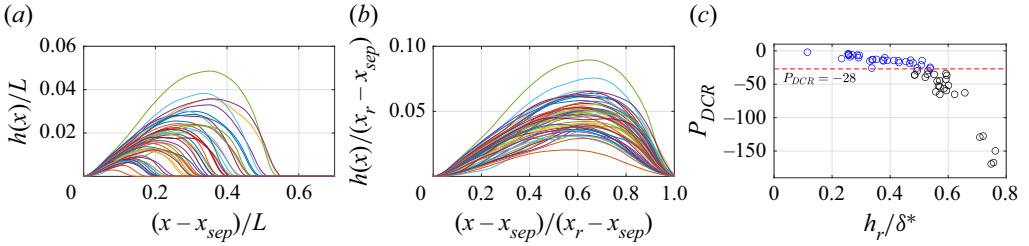

Figure 3. (*a*) Dividing streamlines scaled with the plate length (h/L) and centred on the separation position for all combinations of Re_L, *AP* and *Tu* levels; (*b*) dividing streamlines scaled with the bubble length both on streamwise and wall-normal coordinates; (*c*) bursting parameter (P_{DCR}) as a function of the non-dimensional recirculating height of the bubble (h_r/δ^*). The bursting threshold $P_{DCR} = -28$ proposed by Diwan *et al.* (2006) is shown with red dashed line. Long and short bubbles are highlighted with black and blue colour, respectively.

height of the LSB are scaled with the distance between the reattachment and the separation positions ($x_r - x_{sep}$) showing the height-to-length variation of LSBs. The current data highlight a marked change in bubble dimensions over the investigated parameter space, ranging from relatively thin and short bubbles to separated flow regions extending over most of the test-plate surface (see e.g. figure 2*b*). To verify the occurrence of short- and long-bubble regimes within the present database, the bursting parameter $P_{DCR} = (h^2/\nu)(\Delta U/\Delta X)_{act}$ originally introduced by Diwan *et al.* (2006) was employed. Here, h is the maximum height of the separating streamline of the bubble, ν is the kinematic viscosity and $(\Delta U/\Delta X)_{act}$ is the actual velocity gradient between the separation and the reattachment positions. Figure 3(*c*) reports the P_{DCR} for all cases examined, which is plotted vs the maximum height of the recirculating flow region (h_r). Here, h_r is scaled with the local displacement thickness (δ^*). The results show that a significant subset of data P_{DCR} falls below the bursting threshold of -28 proposed by Diwan *et al.* (2006) to delineate between the short- and long-bubble regimes. It has been also shown in Rist & Maucher (1994) that $h_r/\delta^* = 0.6$ marks the occurrence of an absolute instability in LSBs, which is typical of the long-bubble regime (Sengupta *et al.* 2019). The present results show a progressive increase in h_r/δ^* with decreasing P_{DCR} below the bursting threshold, where h_r/δ^* eventually exceeds 0.6. The analysis carried out in § 4 is aimed at providing a reduced-order representation of the two-dimensional bubble topology towards a common scaling.

4. POD decomposition of the time-mean data ensemble

The POD (Lumley 1970) was used to decompose a mean flow snapshot matrix, whose columns contain the wall-normal coordinates of the points providing the dividing streamline for all Re_L values, *Tu* levels and pressure gradients investigated. Consequently, the POD modes capture the variance of the time-mean shape of the bubble through the entire data set, whereas the coefficients incorporate the effects of varying flow parameters. The first three POD modes (ϕ) so derived and the corresponding coefficients (χ) are reported in figures 4(*a*) and 4(*b*), respectively. These three modes capture approximately 98 % of the overall variance of the data set. A mode convergence analysis was performed to ensure the convergence of modes 1, 2 and 3, and all three modes were observed to reach adequate convergence ($\geq$95 %) when only 20 % of the data were considered. It is also mentioned here that the dividing streamlines were sorted in the data matrix based on the corresponding Re_L values at fixed pressure gradient and *Tu* levels. This is the

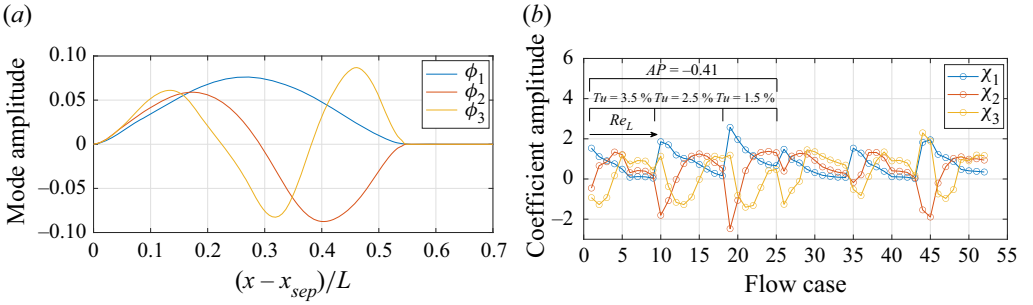

Figure 4. (*a*) First three POD modes and (*b*) corresponding coefficients. The Reynolds number variation is incorporated in each of the six blocks corresponding to a given combination of *Tu* level and pressure gradient.

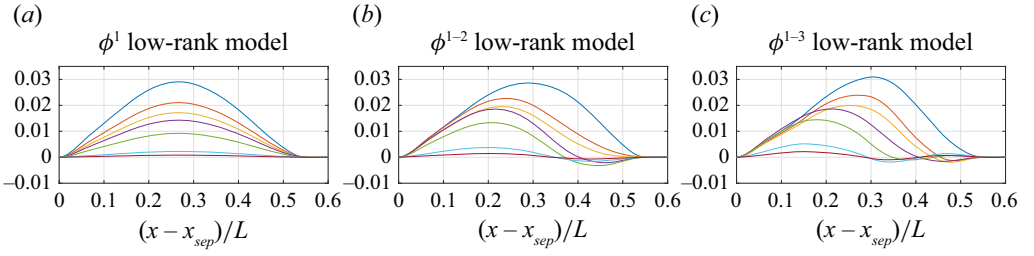

Figure 5. Low-rank reconstruction of dividing streamlines for different Re_L values at constant *Tu* level and pressure gradient. Mean flow data are reconstructed using mode 1 (ϕ^1, *a*), modes 1 and 2 (ϕ^{1-2}, *b*) and modes 1 to 3 (ϕ^{1-3}, *c*).

cause of the repeating data segment patterns in the POD coefficients seen in figure 4(*b*). The POD coefficients represent the relative contribution of the corresponding modes to the reconstruction of each individual record of the data ensemble. The first mode depicted in figure 4(*a*) is representative of the mean dividing streamline of the overall data set. Once combined with the related coefficient, this mode provides the scaling of the bubble height due to the flow parameter variation, with the Reynolds number playing a major role in this sense. Particularly, χ_1 exhibits a piece-wise descending behaviour with constant positive sign. It retains the expected bubble size reduction due the increment of the flow Reynolds number: Re_L increases from left to right in figure 4(*b*) for each of the six blocks constituting the overall coefficients. Modes 2 and 3 are instead representative of the deformation of the bubble shape rather than its scaling, with their related coefficients showing the occurrence of stationary points and sign change. More precisely, mode 2 acts to adjust the shape of the ensemble average mode, depending on the sign and magnitude of the corresponding coefficient. The same role is ascribed to mode 3, which exhibits a higher-order wavelength and lower-energy content, following the POD modes ranking.

To illustrate the interaction of the leading three modes in defining the time-average shape of the LSB, figure 5 reports the low-rank representation of a subset of dividing streamlines for different Reynolds numbers at a fixed *Tu* level and pressure gradient (seven flow cases within the first block depicted in figure 4(*b*) are shown). In figure 5(*a*), the original data are reconstructed using the 1st POD mode only. Its utility is clearly linked to the scaling of the bubble height. When the contributions of modes 2 and 3 are added to the reconstructed data (figure 5*b*,*c*), a modification of the maximum height position and, especially, of the bubble geometry near the reattachment region can be observed. Particularly, a marked inflection of the green and the violet curves is seen downstream of

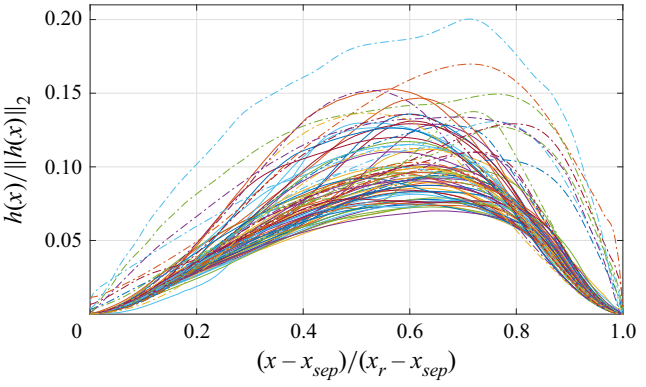

Figure 6. Non-dimensionalized dividing streamlines taken from the current (—) and selected literature (·—) data.

the maximum bubble height. These curves correspond to the 4th and the 5th points of the first block in figure 4(*b*), for which χ_2 (red curve) shows the maximum values. The same behaviour is observed for all the other combinations of the *Tu* level and pressure gradient, each showing a critical Reynolds number at which the deformation of the time-average shape of the bubble captured by mode 2 is maximum. Based on the P_{DCR} parameter reported in figure 3(*c*), the same Re_L values at which the change of the bubble shapes captured by mode 2 occurs was found to be linked to the bursting of the LSB. The present results therefore highlight the link between bubble bursting and characteristic changes of the time-average shape of the bubble.

5. Description of the response of an LSB in the POD space

As discussed in § 4, the *i*th element of a given POD coefficient provides the contribution of the corresponding mode to the *i*th flow case. In the POD subspace constituted by the first three leading modes (figure 4*a*), the *i*th dividing streamline is therefore represented by the triplet of coordinates $\chi_1(i)$, $\chi_2(i)$, $\chi_3(i)$, which are obtained by projection. Since the first three POD modes capture the modification of the bubble shape due to Reynolds number, *Tu* level, and pressure gradient variation, they can be used to define a low-order state space describing the response of an LSB shape to changes in the main influencing parameters. Data projection on the present POD space is also expected to increase the capability of detecting the modification of the statistical response of the bubble between the short and the long regimes.

In the present work, the projection of the current data was considered together with experimental results previously reported in the literature: Simoni *et al.* (2019), Simoni *et al.* (2017), Istvan & Yarusevych (2018), Toppings & Yarusevych (2022) and Aniffa *et al.* (2023). These studies describe LSBs forming over flat plates and airfoils under different *Tu* levels, pressure gradients and angles of attack. In order to make the current and literature data comparable, the 1-D vectors containing the wall-normal coordinates of the dividing streamlines were normalized with their corresponding L_2 norm ($||\cdot||_2$). Here L_2-normalization eliminates the bias due to considering different geometrical parameters for the scaling of an LSB, i.e. plate length or airfoil chord. Figure 6 shows the acquired dividing streamlines (continuous lines) together with literature data (dash-dotted lines) with unitary norm. Data are plotted against the normalized length of the recirculating region highlighting the variation of the shape of the LSBs within the present enlarged

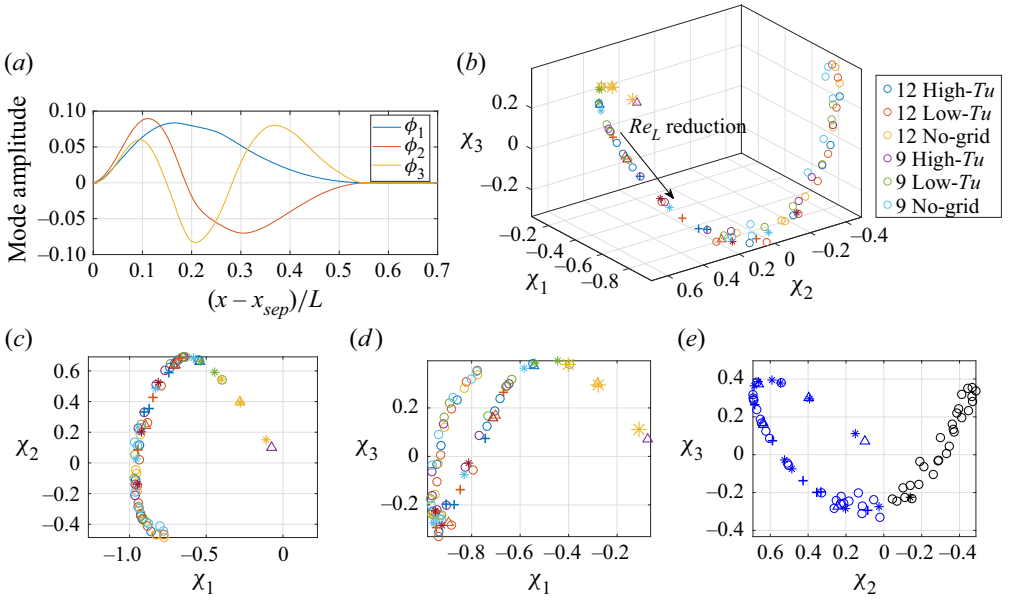

Figure 7. (*a*) The POD modes of normalized dividing streamlines; (*b*) 3-D plot of POD coefficients χ_1, χ_2, χ_3, current data set, (○); Simoni *et al.* (2019), (+); Simoni *et al.* (2017), (∗); Istvan & Yarusevych (2018) and Toppings & Yarusevych (2022), (△); and Aniffa *et al.* (2023), (∗); (*c*) 2-D plot of χ_1-χ_2 coefficients; (*d*) 2-D plot of χ_1-χ_3 coefficients; (*e*) 2-D plot of χ_2-χ_3 coefficients (long and short bubbles are highlighted with black and blue colour, respectively).

database. Regardless of the curve scatter observed in figure 6, the projection of all data on the POD space computed from the current database showed the existence of an underlying principal response of an LSB to changes in the influencing parameters.

Figure 7(*a*) shows the POD modes adopted for projection that are computed from the current dividing streamlines with unitary L_2 norm. Note that the shape of POD modes and their role in reconstructing the LSB shape with L_2-normalization are the same as those obtained using global geometric scaling in figures 4 and 5. Figure 7(*b*) shows a 3-D plot of the first three POD coefficients obtained from projection of the present database and experimental results previously reported in the literature. These latter pertain to different combinations of governing parameters and have not been used to construct the present POD space, which qualifies them as validation sets. It should be stressed that the coefficients reported in figure 7(*b*) are obtained by projection of L_2-normalized data and are consequently distinct from those reported in figure 4(*b*). The results show that all data fall on a well-defined path once projected into the present POD state space (figure 7*b*), with the Reynolds number governing the bubble response. Data acquired for different *Tu* levels, pressure gradients and surface geometries collapse well with higher scatter observed near the minimum value of χ_3 (see figure 7*c–e*). The present results therefore indicate the existence of a general response of the time-mean shape of LSBs to the variation of the main influencing parameters that is captured by the leading POD modes. Based on the P_{DCR} parameter, short and long bubbles are indicated in figure 7(*e*) with blue and black colour, respectively. The results demonstrate that the region in the current state space characterized by $\chi_2 < 0$ pertains to long LSBs, thus the second POD coefficient can be employed for the data-driven classification of the bubble regime. It is stressed that the classification of the bubble state should be performed considering the POD modes

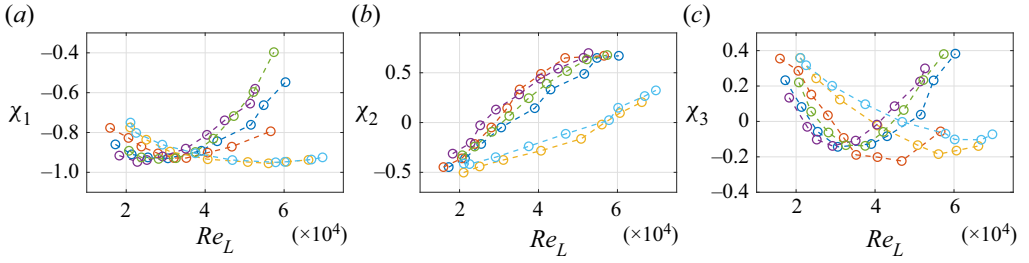

Figure 8. Influence of Re_L on the projection coefficients (*a*) χ_1, (*b*) χ_2 and (*c*) χ_3 for the different AP and *Tu* levels. For the colour legend refer to figure 7(*b*).

obtained by the current entire database, which was seen to retain flow features of both short- and long-bubble configurations. Results from other studies, which pertain to short LSBs, lie on the same trajectory as described by the currently acquired short LSBs. Since the first three POD coefficients were shown to capture the change in the bubble length and height due to the variation of flow parameters, the abrupt change of the trajectory defined by the leading coefficients near the minimum value of χ_3 is representative of a substantial change in the scaling law of an LSB when Re_L decreases below a bursting threshold. The notably lower data scatter in the short regime indicates that a well-defined correlation may exist between the change of the bubble height (governed by mode 1, figure 4*a*) and length (governed by modes 2 and 3, figure 4*a*). On the other hand, higher data dispersion observed for the long state reflects an increased sensitivity of long-bubble shape to the modification of flow properties, such as the *Tu* level and the pressure gradient.

For the sake of completeness, figure 8 shows the influence of Re_L on the first three POD coefficients at fixed AP and *Tu* level. The trajectory defined by each POD coefficient is traversed in a smooth manner when changing the flow parameters. Also, expected trends are observed based on the known physical response of LSBs to changes in the flow parameters. The value of Re_L at which χ_2 becomes negative reduces when increasing the *Tu* level and/or decreasing the magnitude of the adverse pressure gradient. Higher levels of free-stream turbulence promote the shear-layer transition, thus shortening the length of an LSB. Similarly, reducing the adverse pressure gradient magnitude results in a thinner separated flow region. In both cases, LSB bursting is delayed to lower Re_L.

6. Conclusions

The present work presents a data-driven analysis of the response of a flat-plate LSB to changes in the influencing parameters. The Reynolds number, *Tu* level and pressure gradient were changed to produce short and long LSBs. The POD was applied to the data matrix constituted by the wall-normal coordinates of all dividing streamlines. The leading three POD modes were shown to capture the essential bubble geometry within the current database. The projection of data from the current and prior investigations into the state space constituted by the leading three modes revealed the existence of a low-order response of the normalized time-mean structure of an LSB to changes in the flow parameter, which was expressed in terms of modification of the separating streamline of the bubble. It was found that flat plate and airfoil LSBs that were not used for the computation of the modes collapse onto the trajectory defined by the present POD coefficients. The high collapse of data concerning short LSBs indicate a marked correlation between the change in the bubble maximum height and length captured by the current POD modes. Contrarily, the

increased data dispersion in the long regime suggests that long bubbles are more sensitive to the variation of the external flow disturbances and the pressure gradient. It was shown that the POD space derived from the current set of measurements can be adopted for the unsupervised clustering of short and long LSBs.

Declaration of interests. The authors report no conflict of interest.

Author ORCIDs.
M. Dellacasagrande https://orcid.org/0000-0002-9383-9600;
D. Lengani https://orcid.org/0000-0001-6347-0817;
D. Simoni https://orcid.org/0000-0003-4161-0721;
S. Yarusevych https://orcid.org/0000-0003-2723-2744.

References

Alam, M. & Sandham, N. 2000 Direct numerical simulation of 'short' laminar separation bubbles with turbulent reattachment. *J. Fluid Mech.* **410**, 1–28.

Alizard, F., Cherubini, S. & Robinet, J.-C. 2009 Sensitivity and optimal forcing response in separated boundary layer flows. *Phys. Fluids* **21** (6), 064108.

Allen, T. & Riley, N. 1995 Absolute and convective instabilities in separation bubbles. *Aeronaut. J.* **99** (990), 439–449.

Aniffa, S.M., Caesar, V.S., Dabaria, V. & Mandal, A.C. 2023 Characteristics of geometry-and pressure-induced laminar separation bubbles at an enhanced level of free-stream turbulence. *J. Fluid Mech.* **957**, A19.

Balzer, W. & Fasel, H.F. 2016 Numerical investigation of the role of free-stream turbulence in boundary-layer separation. *J. Fluid Mech.* **801**, 289–321.

Boutilier, M.S.H. & Yarusevych, S. 2012 Parametric study of separation and transition characteristics over an airfoil at low Reynolds numbers. *Exp. Fluids* **52** (6), 1491–1506.

Cherubini, S., Robinet, J.-Ch. & De Palma, P. 2010*a* The effects of non-normality and nonlinearity of the Navier–Stokes operator on the dynamics of a large laminar separation bubble. *Phys. Fluids* **22** (1), 014102.

Cherubini, S., Robinet, J.-Ch., De Palma, P. & Alizard, F. 2010*b* The onset of three-dimensional centrifugal global modes and their nonlinear development in a recirculating flow over a flat surface. *Phys. Fluids* **22** (11), 114102.

Dellacasagrande, M., Barsi, D., Lengani, D., Simoni, D. & Verdoya, J. 2020 Response of a flat plate laminar separation bubble to Reynolds number, free-stream turbulence and adverse pressure gradient variation. *Exp. Fluids* **61** (6), 128.

Diwan, S.S., Chetan, S.J. & Ramesh, O.N. 2006 On the bursting criterion for laminar separation bubbles. In *IUTAM Symposium on Laminar-Turbulent Transition* (ed. R. Govindarajan), pp. 401–407. Springer.

Ehrenstein, U. & Gallaire, F. 2008 Two-dimensional global low-frequency oscillations in a separating boundary-layer flow. *J. Fluid Mech.* **614**, 315–327.

Eljack, E., Soria, J., Elawad, Y. & Ohtake, T. 2021 Simulation and characterization of the laminar separation bubble over a NACA-0012 airfoil as a function of angle of attack. *Phys. Rev. Fluids* **6** (3), 034701.

Embacher, M. & Fasel, H.F. 2014 Direct numerical simulations of laminar separation bubbles: investigation of absolute instability and active flow control of transition to turbulence. *J. Fluid Mech.* **747**, 141–185.

Fasel, H.F. & Postl, D. 2006 Interaction of separation and transition in boundary layers: direct numerical simulations. In *IUTAM Symposium on Laminar-Turbulent Transition* (ed. R. Govindarajan), pp. 71–88. Springer.

Gaster, M. 1967 The structure and behaviour of laminar separation bubbles. *Tech. Rep.* 3595. Aeronautical Research Council.

Hammond, D.A. & Redekopp, L.G. 1998 Local and global instability properties of separation bubbles. *Eur. J. Mech. (B/Fluids)* **17** (2), 145–164.

Horton, H.P. 1967 *A Semi-Empirical Theory for the Growth and Bursting of Laminar Separation Bubbles*. H.M. Stationery Office.

Hosseinverdi, S. & Fasel, H.F. 2019 Numerical investigation of laminar–turbulent transition in laminar separation bubbles: the effect of free-stream turbulence. *J. Fluid Mech.* **858**, 714–759.

HUERRE, P. & MONKEWITZ, P.A. 1990 Local and global instabilities in spatially developing flows. *Annu. Rev. Fluid Mech.* **22** (1), 473–537.

ISTVAN, M.S. & YARUSEVYCH, S. 2018 Effects of free-stream turbulence intensity on transition in a laminar separation bubble formed over an airfoil. *Exp. Fluids* **59** (3), 52.

JAROSLAWSKI, T., FORTE, M., VERMEERSCH, O., MOSCHETTA, J.-M. & GOWREE, E.R. 2023 Disturbance growth in a laminar separation bubble subjected to free-stream turbulence. *J. Fluid Mech.* **956**, A33.

KURELEK, J.W., TUNA, B.A., YARUSEVYCH, S. & KOTSONIS, M. 2021 Three-dimensional development of coherent structures in a two-dimensional laminar separation bubble. *AIAA J.* **59** (2), 493–505.

LUMLEY, J.L. 1970 *Stochastic Tools in Turbulence*. Applied Mathematics and Mechanics, vol. 12. Academic Press.

MARQUILLIE, M. & EHRENSTEIN, U.W.E. 2003 On the onset of nonlinear oscillations in a separating boundary-layer flow. *J. Fluid Mech.* **490**, 169–188.

MARXEN, O. & HENNINGSON, D.S. 2011 The effect of small-amplitude convective disturbances on the size and bursting of a laminar separation bubble. *J. Fluid Mech.* **671**, 1–33.

MARXEN, O., LANG, M. & RIST, U. 2013 Vortex formation and vortex breakup in a laminar separation bubble. *J. Fluid Mech.* **728**, 58–90.

MARXEN, O. & RIST, U. 2010 Mean flow deformation in a laminar separation bubble: separation and stability characteristics. *J. Fluid Mech.* **660**, 37–54.

MICHELIS, T., YARUSEVYCH, S. & KOTSONIS, M. 2017 Response of a laminar separation bubble to impulsive forcing. *J. Fluid Mech.* **820**, 633–666.

MITRA, A. & RAMESH, O.N. 2019 New correlation for the prediction of bursting of a laminar separation bubble. *AIAA J.* **57** (4), 1400–1408.

NAKAMURA, Y., OHYA, Y. & TSURUTA, H. 1991 Experiments on vortex shedding from flat plates with square leading and trailing edges. *J. Fluid Mech.* **222**, 437–447.

PAULEY, L.L., MOIN, P. & REYNOLDS, W.C. 1990 The structure of two-dimensional separation. *J. Fluid Mech.* **220**, 397–411.

PRÖBSTING, S. & YARUSEVYCH, S. 2015 Laminar separation bubble development on an airfoil emitting tonal noise. *J. Fluid Mech.* **780**, 167–191.

RIST, U. & MAUCHER, U. 1994 Direct numerical simulation of 2-D and 3-D instability waves in a laminar separation bubble. In *Proc.of the AGARD Symposium on Application of Direct and Large Eddy Simulation to Transition and Turbulence, AGARD-CP-551, Chania, Crete*. Elsevier.

RIST, U. & MAUCHER, U. 2002 Investigations of time-growing instabilities in laminar separation bubbles. *Eur. J. Mech. (*B*/Fluids)* **21** (5), 495–509.

RODRÍGUEZ, D., GENNARO, E.M. & SOUZA, L.F. 2021 Self-excited primary and secondary instability of laminar separation bubbles. *J. Fluid Mech.* **906**, A13.

SANDHAM, N.D. 2008 Transitional separation bubbles and unsteady aspects of aerofoil stall. *Aeronaut. J.* **112** (1133), 395–404.

SCIACCHITANO, A., NEAL, D.R., SMITH, B.L., WARNER, S.O., VLACHOS, P.P., WIENEKE, B. & SCARANO, F. 2015 Collaborative framework for PIV uncertainty quantification: comparative assessment of methods. *Meas. Sci. Technol.* **26** (7), 074004.

SENGUPTA, T.K., SHARMA, P.K., SENGUPTA, A. & SUMAN, V.K. 2019 Tracking disturbances in transitional and turbulent flows: coherent structures. *Phys. Fluids* **31** (12), 124106.

SERNA, J. & LÁZARO, B.J. 2015 On the bursting condition for transitional separation bubbles. *Aerosp. Sci. Technol.* **44**, 43–50.

SIMONI, D., LENGANI, D., DELLACASAGRANDE, M., KUBACKI, S. & DICK, E. 2019 An accurate data base on laminar-to-turbulent transition in variable pressure gradient flows. *Intl J. Heat Fluid Flow* **77**, 84–97.

SIMONI, D., LENGANI, D., UBALDI, M., ZUNINO, P. & DELLACASAGRANDE, M. 2017 Inspection of the dynamic properties of laminar separation bubbles: free-stream turbulence intensity effects for different Reynolds numbers. *Exp. Fluids* **58** (6), 66.

TOPPINGS, C.E. & YARUSEVYCH, S. 2022 Structure and dynamics of a laminar separation bubble near a wing root: towards reconstructing the complete lsb topology on a finite wing. *J. Fluid Mech.* **944**, A14.

VERDOYA, J., DELLACASAGRANDE, M., LENGANI, D., SIMONI, D. & UBALDI, M. 2021 Inspection of structures interaction in laminar separation bubbles with extended proper orthogonal decomposition applied to multi-plane particle image velocimetry data. *Phys. Fluids* **33** (4), 043607.